



Detection of Water Vapor in the Thermal Spectrum of the Non-transiting Hot Jupiter Upsilon Andromedae b

Danielle Piskorz¹, Björn Benneke^{1,2}, Nathan R. Crockett¹ , Alexandra C. Lockwood³, Geoffrey A. Blake¹ ,
Travis S. Barman⁴ , Chad F. Bender⁵ , John S. Carr⁶ , and John A. Johnson⁷

¹ Division of Geological and Planetary Sciences, California Institute of Technology, Pasadena, CA 91125, USA; dpiskorz@gps.caltech.edu

² Instituté for Research on Exoplanets, Université de Montréal, Montreal, Canada

³ Space Telescope Science Institute, Baltimore, MD 21218, USA

⁴ Lunar and Planetary Laboratory, University of Arizona, Tucson, AZ 85721, USA

⁵ Department of Astronomy and Steward Observatory, University of Arizona, Tucson, AZ 85721, USA

⁶ Naval Research Laboratory, Washington, DC 20375, USA

⁷ Harvard-Smithsonian Center for Astrophysics; Institute for Theory and Computation, Cambridge, MA 02138, USA

Received 2017 February 22; revised 2017 June 16; accepted 2017 July 2; published 2017 August 1

Abstract

The Upsilon Andromedae system was the first multi-planet system discovered orbiting a main-sequence star. We describe the detection of water vapor in the atmosphere of the innermost non-transiting gas giant ups And b by treating the star–planet system as a spectroscopic binary with high-resolution, ground-based spectroscopy. We resolve the signal of the planet’s motion and break the mass-inclination degeneracy for this non-transiting planet via deep combined flux observations of the star and the planet. In total, seven epochs of Keck NIRSPEC *L* band observations, three epochs of Keck NIRSPEC short-wavelength *K* band observations, and three epochs of Keck NIRSPEC long wavelength *K* band observations of the ups And system were obtained. We perform a multi-epoch cross-correlation of the full data set with an atmospheric model. We measure the radial projection of the Keplerian velocity ($K_P = 55 \pm 9 \text{ km s}^{-1}$), true mass ($M_b = 1.7^{+0.33}_{-0.24} M_J$), and orbital inclination ($i_b = 24^\circ \pm 4^\circ$), and determine that the planet’s opacity structure is dominated by water vapor at the probed wavelengths. Dynamical simulations of the planets in the ups And system with these orbital elements for ups And b show that stable, long-term (100 Myr) orbital configurations exist. These measurements will inform future studies of the stability and evolution of the ups And system, as well as the atmospheric structure and composition of the hot Jupiter.

Key words: planets and satellites: atmospheres – techniques: spectroscopic

1. Introduction

The first exoplanet in the upsilon Andromedae system was discovered in 1997 with the radial velocity (RV) technique (Butler et al. 1997). Two more years of RV observations revealed the presence of two additional planets in the system, making ups And the first multiple exoplanet system discovered around a main-sequence star (Butler et al. 1999). Three planets orbit the F star ups And A: (1) ups And b, a hot Jupiter with a minimum mass of $0.71M_J$ and a period of 4.617 ± 0.0003 days, (2) ups And c, a gas giant with a minimum mass of $2.11M_J$ orbiting with a period of 241.2 ± 1.1 days and an eccentricity of 0.18 ± 0.11 , and (3) ups And d, another gas giant having a minimum mass of $4.61M_J$ orbiting with a period of 1266.6 ± 30 days and an eccentricity of 0.41 ± 0.11 . Adding to the intrigue, in 2002, a red dwarf companion ups And B with a projected separation of 750 au from ups And A was detected and determined to have negligible effects on RV observations (Lowrance et al. 2002).

This unique assemblage spurred a torrent of investigations into the origin and stability of the system, a few of which we mention here. Adams & Laughlin (2006) showed that the inclusion of general relativity was required to explain the short period and small eccentricity of ups And b. Were it not for general relativity, ups And b would precess slowly and its eccentricity would be pumped by the massive outer planets. Depending on the mutual inclinations of the planets in the system, it is possible that the Kozai–Lidov mechanism is responsible for the short-period orbit of ups And b (Nagasawa

et al. 2008), while Lissaeur & Rivera (2001) suggested that the present-day dynamics of ups And b may be detached from that of the outer planets. Chiang & Murray (2002) suggested that if the orbital planes of ups And c and d were coplanar and locked in an apsidal resonance, then the eccentricity of ups And d would be pumped over time as the apsidal resonance damped. Once the apsides are aligned, secular interactions would cause eccentricity to be transferred from ups And d to ups And c. Barnes & Greenberg (2006) determined that ups And c and d lie near the separatrix between libration and circulation, though this behavior could not be explained by planet–planet scattering (Barnes & Greenberg 2007).

For lack of complete ephemerides, many of these works assumed that the planets’ minimum masses were their true masses in their models, and therefore that the system was coplanar. A notable exception was Rivera & Lissaeur (2000) who concluded that scattering or ejections is a likely cause of the outer planets’ high eccentricities. In all, one statement can summarize many of these works: the ups And A system is on the edge of instability.

Determining the masses and inclinations of ups And A’s planets is critical for realistic interpretations of the system’s origin and stability. Five $24 \mu\text{m}$ Spitzer observations of ups And b suggested $i_b > 30^\circ$ (Harrington et al. 2006). To that, Crossfield et al. (2010) added seven individual and 28 continuous hours of $24 \mu\text{m}$ Spitzer observations to further constrain $i_b > 28^\circ$. This work also reported that the flux maximum for ups And b occurred 80° before opposition, an observation inconsistent with atmospheric circulation models.

Table 1
 μ And System Properties

Property	Value	References
μ And A		
Mass, M_*	$1.31 \pm 0.02 M_\odot$	(1)
Radius, R_*	$1.64^{+0.04}_{-0.05} R_\odot$	(1)
Effective temperature, T_{eff}	6213 ± 44 K	(2)
Metallicity, [Fe/H]	0.13 ± 0.07	(3)
Surface gravity, $\log g$	4.25 ± 0.06	(2)
Rotational velocity, $v \sin i$	9.62 ± 0.5 km s ⁻¹	(2)
Systemic velocity, v_{sys}	-28.59 km s ⁻¹	(4)
K band magnitude, K_{mag}	2.86 ± 0.08	(5)
μ And b		
Velocity semi-amplitude, K	70.51 ± 0.37 m s ⁻¹	(6)
Line-of-sight orbital velocity, K_p	55 ± 9 km s ⁻¹	(7)
Indicative mass, $M \sin(i)$	$0.69 \pm 0.02 M_J$	(6)
Mass, M_p	$1.7^{+0.33}_{-0.24} M_J$	(7)
Inclination, i	$24^\circ \pm 4^\circ$	(7)
Semimajor axis, a	0.0594 ± 0.0003 au	(6)
Period, P	4.617111 ± 0.000014 days	(6)
Eccentricity, e	0.012 ± 0.005	(6)
Argument of periastron, ω	$44^\circ.11 \pm 25^\circ.56$	(6)
Time of periastron, t_{peri}	2450034.05 ± 0.33 JD	(6)
Phase uncertainty, $\sigma_{f+\omega}$	$0^\circ.9$	(7)
μ And c		
Mass, M_p	$13.98^{+2.3}_{-5.3} M_J$	(6)
Inclination, i	$7^\circ.868 \pm 1^\circ.003$	(6)
Semimajor axis, a	0.8259 ± 0.043 au	(6)
Period, P	240.9402 ± 0.047 days	(6)
Eccentricity, e	0.245 ± 0.006	(6)
Argument of periastron ^a , ω	$10^\circ.81 \pm 7^\circ.73$	(6)
Longitude of periastron, ϖ	$247^\circ.66 \pm 1^\circ.76$	(6)
Longitude of ascending node, Ω	$236^\circ.85 \pm 7^\circ.53$	(6)
Time of periastron, t_{peri}	2449922.53 ± 1.17 JD	(6)
μ And d		
Mass, M_p	$10.25^{+0.7}_{-3.3} M_J$	(6)
Inclination, i	$23^\circ.758 \pm 1^\circ.316$	(6)
Semimajor axis, a	2.53 ± 0.014 au	(6)
Period, P	1281 ± 1.055 days	(6)
Eccentricity, e	0.316 ± 0.006	(6)
Argument of periastron ^a , ω	$248^\circ.92 \pm 3^\circ.55$	(6)
Longitude of periastron, ϖ	$252^\circ.99 \pm 1^\circ.31$	(6)
Longitude of ascending node, Ω	$4^\circ.07 \pm 3^\circ.30$	(6)
Time of periastron, t_{peri}	2450059.38 ± 3.50 JD	(6)

Note.

^a We calculate the argument of periastron from the values of longitude of periastron and longitude of the ascending node reported in McArthur et al. (2010). We calculate the error bars on the longitude of periastron by combining the reported error bars on the argument of periastron and the longitude of the ascending node in quadrature.

References. (1) Takeda et al. (2007); (2) Valenti & Fischer (2005); (3) Gonzalez & Laws (2007); (4) Nidever et al. (2002); (5) anBelle & vonBraun (2009); (6) McArthur et al. (2010); (7) This work.

McArthur et al. (2010) used a combination of high-precision astrometry taken with the Fine Guidance Sensor on the *Hubble Space Telescope* and a large RV data set (974 observations taken over 14 years) to determine all the orbital elements of ups And c and d and provide some insight into the orbital elements of ups And b. ups And c was shown to have a mass of $14M_J$ and inclination of 8° from face-on while ups And d has a mass of $10M_J$ and an inclination of 24° from face-on. (See Table 1 for all reported orbital elements with error bars.) The

mutual inclination of ups And c and d is about 30° . McArthur et al. (2010) made no astrometric detection of ups And b, indicating that its inclination must be greater than $1^\circ.2$. They also postulated the presence of a fourth planet in the system in resonance with the third planet and determined that the stellar companion ups And B was indeed bound with a true separation of ~ 9900 au. The existence of the fourth planet ups And d was further supported by Curiel et al. (2011). A non-Newtonian simulation of the system suggested that ups And b had an inclination less than $\sim 60^\circ$ or greater than $\sim 135^\circ$.

Drawing on the results of McArthur et al. (2010), Dietrick et al. (2015) ran post-Newtonian numerical simulations of the system to determine which masses and inclinations of ups And b would allow the system as a whole to be stable. The system has a general “region of stability” when $i_b < 40^\circ$. Specifically, Dietrick et al. (2015) investigated four stable, prograde simulations having $i_b < 25^\circ$, but precise conclusions on the mass and inclination of the innermost planet have eluded astronomers.

Ground-based high-resolution spectroscopy techniques have successfully broken the degeneracy between mass and inclination for non-transiting planets and would be ideal for determining the mass and inclination of ups And b. These techniques treat the target star and its planet as if they were a spectroscopic binary, teasing out the line-of-sight Keplerian velocity of the planet as it orbits the star (Snellen et al. 2010). In addition to untangling the mass and inclinations of bright planets, this technique also gives information on atmospheric composition (Brogi et al. 2012, 2013, 2014; de Mooij et al. 2012; Rodler et al. 2012; Birkby et al. 2013; de Kok et al. 2013; Lockwood et al. 2014; Martins et al. 2015; Piskorz et al. 2016), wind speed (Snellen et al. 2014), and length of day (Schwarz et al. 2015; Brogi et al. 2016) and has been carried out using CRIRES at VLT, HARPS at ESO-La Silla, and NIRSPEC at Keck. Observers using CRIRES (e.g., Snellen et al. 2010) or HARPS (e.g., Martins et al. 2015) tend to allow the planet lines to smear across the detector over the course of many hours. Observers using NIRSPEC (e.g., Lockwood et al. 2014) take up to two hour long snapshots of the planet’s emission spectrum at various phases of the planet’s orbit. Since NIRSPEC has a resolution of 25,000–30,000 at the observed wavelengths, planet lines generally do not smear across pixels during a 2–3 hr observation. Owing to NIRSPEC’s cross-dispersed echelle format, this method yields many planet lines spread over many orders, producing sufficient signal-to-noise to detect the planet’s atmosphere.

In this paper, we use NIRSPEC observations and the methods presented in Piskorz et al. (2016) to discern the true mass, inclination, and atmospheric composition of the hot Jupiter ups And b. An important divergence from the method presented in Piskorz et al. (2016) is the inclusion of K band data taken with two different echelle settings, accessing planetary features across the full K band. In Section 2, we detail our NIRSPEC observations, data reduction, and telluric correction, while Section 3 describes the cross-correlation analysis and maximum likelihood calculation of the orbital solution for ups And b. In Section 4, we discuss the robustness of our orbital solution, the long-term stability of the ups And A system, insights into the atmosphere of ups And b, and give some notes on the observations.

Table 2
NIRSPEC Observations of ups And b

Date	Modified Julian Date ^a (−2400,000.5 days)	Mean Anomaly M^b (2π rad)	Barycentric Velocity v_{bary} (km s^{-1})	Integration Time (min)	$S/N_{L,K}^c$
<i>L Band (3.0–3.4 μm)</i>					
2011 Sep 6	55810.639	0.25	21.07	60	5376
2011 Sep 7	55811.637	0.46	20.82	10 ^d	2661
2011 Sep 9	55813.509	0.87	20.33	100	8265
2013 Oct 27	56592.526	0.59	1.89	140	9173
2013 Oct 29	56594.512	0.02	0.99	140	5937
2013 Nov 7	56603.609	0.99	−3.17	180	8686
2014 Oct 7	56937.553	0.32	10.64	50	5641
<i>K_r Band (Long Wavelength Side of 2.0–2.4 μm)</i>					
2016 Sep 19	57650.361	0.73	17.14	100	11517
2016 Nov 12	57704.265	0.38	−5.37	230	12872
2016 Dec 15	57737.300	0.53	−18.63	70	7666
<i>K_l Band (Short Wavelength Side of 2.0–2.4 μm)</i>					
2014 Oct 5	56935.579	0.87	11.47	70	7764
2016 Aug 21	57621.589	0.45	24.15	30	4369
2016 Sep 19	57650.501	0.73	17.14	120	10649

Notes.

^a Julian date refers to the middle of the observing sequence.

^b We list only the mean anomalies (and no true anomalies) for our observations, since ups And b’s orbit is nearly circular.

^c S/N_L , S/N_{K_r} , and S/N_{K_l} are calculated at 3.0, 2.1325, and 2.1515 μm , respectively. Each S/N calculation is for a single channel (i.e., resolution element) for the whole observation.

^d Because the total integration time on ups And on 2011 September 7 is very short, we do not use principal component analysis to remove the telluric signals (see Section 2.2), and we exclude this epoch from the following analysis.

2. Observations and Data Reduction

2.1. Observations

We used NIRSPEC (Near InfraRed SPECTrometer; McLean et al. 1998) at the Keck Observatory to observe ups And A and b on seven nights (2011 September 6, 7, and 9, 2013 October 27 and 29 and November 7, and 2014 October 7) in L , three nights (2016 September 19, November 12, and December 15) in K_r (the right, long-wavelength half of the dispersed, K band filtered light), and three nights (2014 October 5 and 2016 August 21 and September 19) in K_l (the left, short-wavelength half of the dispersed, K band filtered light). We obtained spectral resolutions of $\sim 25,000$ in L and $\sim 30,000$ in K using the $0''.4 \times 24''$ slit setup and used an ABBA nodding pattern during data acquisition. In the L band, the echelle orders typically cover 3.4038–3.4565/3.2467–3.3069/3.1193–3.1698/2.995–3.044 μm . The echelle orders in the K_r band typically cover 2.38157–2.41566/2.31–2.34284/2.24245–2.27485/2.17894–2.20861/2.11878–2.14639/2.06170–2.08703 μm , while in the K_l band the echelle orders typically cover 2.34238–2.37535/2.27198–2.30374/2.20554–2.23653/2.14362–2.17298/2.08461–2.11312/2.02931–2.05634 μm . Altogether, the two K band setups provide near continuous wavelength coverage across the entire K band. Table 2 gives the details of these 13 observations.

A top-down schematic of ups And b in orbit around ups And A is shown in Figure 1 with the expected orbital phase of each observational epoch marked. Figure 2 shows RV measurements of ups And A taken from Fischer et al. (2014) in comparison with expectations for the line-of-sight velocity of ups And b. We aim to take observations when the line-of-sight velocities of the star and planet are most distinct and when we expect to observe a decent amount of dayside radiation from the planet, thus maximizing the planet flux.

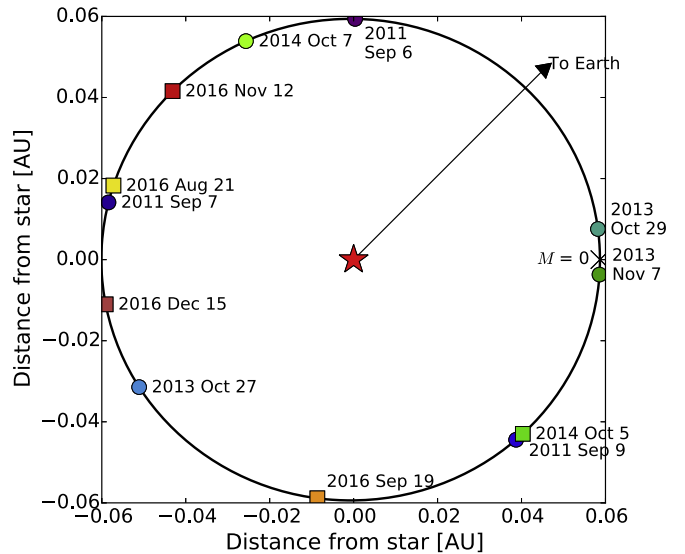


Figure 1. Top-down schematic of the orbit of ups And b around its star according to the orbital parameters derived by McArthur et al. (2010). Each point represents a single epoch of NIRSPEC observations of the system. Circles indicate L band observations and squares represent K band observations. The black arrow represents the line of sight to Earth.

2.2. Extraction of 1D Spectra and PCA-like Telluric Correction

Our data reduction and cleaning methods are parallel to those described in Piskorz et al. (2016) and are summarized here only briefly.

We use a Python pipeline in the style of Boogert et al. (2002) to flat field and dark subtract our data, remove bad pixels, and extract 1D spectra. For the wavelength calibration, we fit a fourth-order polynomial ($\lambda = ax^3 + bx^2 + cx + d$, where x is pixel number and a , b , c , and d are free parameters) that aligns

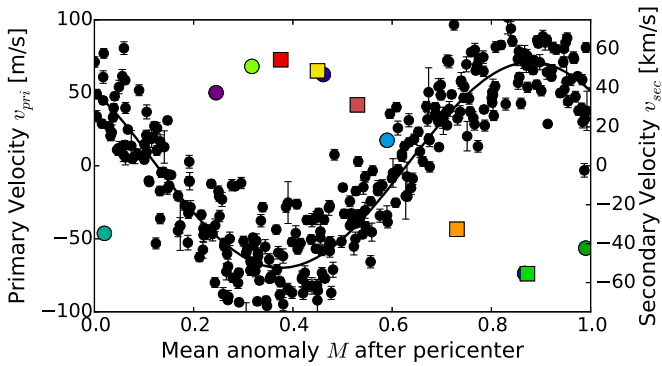


Figure 2. RV data from Fischer et al. (2014) with the best-fit stellar RV (primary velocity) curve overplotted in black, corresponding to the left y-axis. RV contributions from ups And c and d have been removed according to the orbital elements provided in McArthur et al. (2010). The colored points represent the NIRSPEC observations of this planet correspond to the right y-axis and are based on the observation phases and our expectations of their secondary velocities. In this paper, we will show that the most likely value for the Keplerian orbital velocity of ups And b is $55 \pm 9 \text{ km s}^{-1}$.

our L band data to a telluric model or our K band data to a combined telluric and stellar model. Here, the difference in treatment of L and K band data stems from the fact that telluric lines are stronger in the L band than near $2 \mu\text{m}$. Our stellar model is derived from the PHOENIX stellar library (Husser et al. 2013) and is described in more detail in Section 3.1. Finally, we fit an instrument profile to our data as in Valenti et al. (1995) and save it to apply to the models described in Sections 3.1 and 3.2.

We capitalize on the long time series of observations (roughly two minutes per nod, or four minutes per AB pair) taken at each epoch and perform a principal component analysis (PCA) to remove contributions to the spectra from the Earth’s atmosphere. PCA rewrites a data set in terms of its principal components so that the variance of a data set with respect to a model or its mean is reduced. For our purposes, this means that PCA will identify the time-varying components of our time-series data, most notably, changes in the telluric spectrum over the course of a given epoch. The first principal component describes the most variance, the second, the second most, etc. We guide our PCA with a telluric model that best fits the data in terms of water, carbon dioxide, methane, and (where appropriate) ozone abundances, and determine the eigenvectors making up each observed spectrum. We calculate and remove the strongest principal components from our data, leave behind the parts of the spectra that are constant in time (the stellar and planet signals), combine every AB nod of data, and clip regions of substantial telluric absorption ($>75\%$). More information on this technique is given in Piskorz et al. (2016). Figure 3 shows a raw spectrum of ups And taken on 2013 October 29, the first three principal components, and a cleaned spectrum of ups And.

As in our analysis of HD 88133 data, we find that the telluric correction by PCA works well for all orders of L band data, but poorly for the K_r and K_l band orders spanning $2.06170\text{--}2.08703 \mu\text{m}$ and $2.02931\text{--}2.05634 \mu\text{m}$, where there is a dense forest of telluric CO_2 lines. We also find that a few nights of K band observations were contaminated by significant issues with the read-out electronics. In these cases, we exclude the data on the “bad” side of the detector from our analysis; about 25% of the data is on the noisy side of the detector.

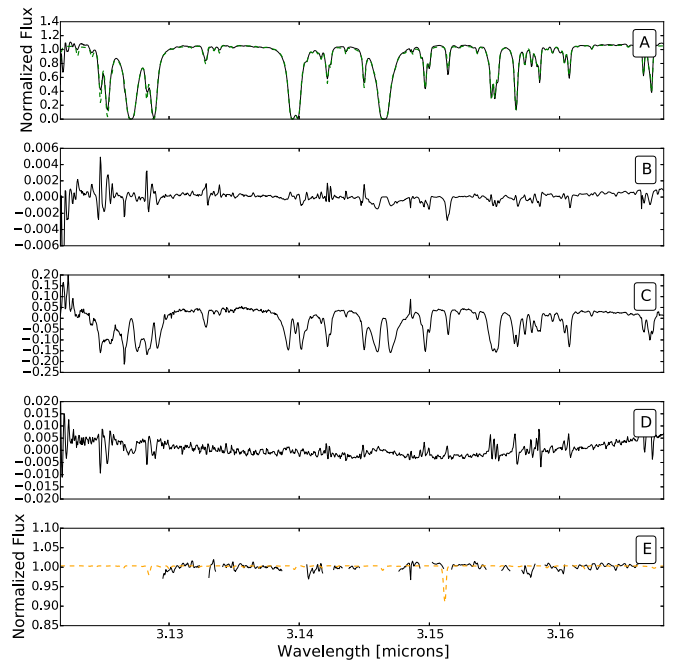


Figure 3. Raw spectrum of ups And, first three principal components, and cleaned spectrum. (A) One order of data from ups And taken on 2013 October 29. The best-fit telluric spectrum is overplotted as a green, dashed line. (B)–(D) The first three principal components in arbitrary units describing changes in air mass, molecular abundances in the Earth’s atmosphere, and plate scale, respectively. (E) Same as (A), but with the first five principal components removed, and with a fitted stellar spectrum overplotted as a dashed, orange line.

Additionally, we remove the 2011 September 7 observations from our data set, since the 10 minute total integration time is not sufficient for PCA.

As in Piskorz et al. (2016), all but about 0.1% of the variance in each night’s data set is encapsulated by the first principal component. The following results are roughly consistent for data sets with more than the first principal component removed. As discussed in Section 4.4 and shown in Figure 7, the expected photometric contrast α_{phot} at the observed wavelengths is $\sim 10^{-6}$. Based on the percent variance removed by each principal component, we determine that deletion of a signal of this magnitude requires the removal of upward of the first 15 principal components from our data. In the analysis that follows, our data set has the first five principal components removed, leaving the stellar and planetary signals intact.

3. Data Analysis and Results

A two-dimensional cross-correlation analysis reveals the ideal velocity shifts for the stellar and planet spectra embedded in our clean data set (Zucker & Mazeh 1994). This analysis calls for accurate stellar and planetary model spectra.

3.1. Model Stellar Spectrum

Our PHOENIX stellar model is interpolated between the spectral grid points presented in Husser et al. (2013) for the effective temperature T_{eff} , surface gravity $\log g$, and metallicity $[\text{Fe}/\text{H}]$ values listed for ups And A in Table 1. We rotationally broaden this model assuming a stellar rotation rate of 9.62 km s^{-1} (Valenti & Fischer 2005) and limb darkening coefficient of 0.29 (Claret 2000). For completeness, we instrumentally broaden the stellar model with the kernel determined in Section 2.2.

3.2. Model Planetary Spectrum

We compute a high-resolution ($R = 250,000$) thermal emission spectrum of ups And b according to the SCARLET framework (Benneke 2015). The thermal structure and equilibrium chemistry of the ups And b model spectrum are dependent upon the expected stellar flux at the location of the planet. The model assumes perfect heat redistribution (perhaps a flawed assumption, see Crossfield et al. 2010 and Section 4.3) and a solar elemental composition (Asplund et al. 2009). The temperature profiles are computed self-consistently for a $1 \times$ solar, $C/O = 0.54$ atmosphere by iteratively recalculating the radiative-convective equilibrium and atmospheric equilibrium chemistry. We assume an internal heat flux of $T_{\text{int}} = 75$ K. Our default model in this paper has an inverted temperature structure due to the short-wavelength absorption of TiO and VO. The SCARLET framework includes molecular opacities of H_2O , CH_4 , NH_3 , HCN , CO , CO_2 , and TiO (ExoMol database by Tennyson & Yurchenko 2012), molecular opacities of O_2 , O_3 , OH , C_2H_2 , C_2H_4 , C_2H_6 , H_2O_2 , and HO_2 (HITRAN database by Rothman et al. 2009), absorptions by alkali metals (VALD database by Piskunov et al. 1995), H_2 -broadening (Burrows & Volobuyev 2003), and collision-induced broadening from H_2/H_2 and H_2/He collisions (Borysow 2002).

Line positions and amplitudes are critical to obtaining the correct cross-correlation function. We use the line information from ExoMol for H_2O and CH_4 . The line lists were computed using ab initio calculations based on quantum mechanics. The line center wavelengths of these calculations are accurate. Line amplitudes are harder to compute in ab initio calculations, but we are using the best state-of-the-art line lists available, which is ExoMol for the temperatures encountered in hot Jupiters. Model spectra are convolved with the instrumental profile from Section 2.2 before the cross-correlation analysis.

3.3. Two-dimensional Cross-correlation

We use the TODCOR algorithm (Zucker & Mazeh 1994) to cross-correlate each order of data for each epoch with the stellar and planet models, yielding a two-dimensional array of cross-correlation values for different stellar and planetary velocity shifts.

As in Piskorz et al. (2016), at this step, we eliminate the K_r and K_l band orders ranging from 2.3 to $2.4 \mu\text{m}$ from the analysis since there is high correlation between the stellar and planetary models themselves at these wavelengths. This means we remove any signal from carbon monoxide, and the dominant molecule in the planetary model in the remaining wavelengths is water vapor.

Following Lockwood et al. (2014), for each epoch of observations, we combine the correlation function for each order and produce nightly stellar and planetary maximum likelihood curves, a few of which are shown in Figure 4. For every epoch, we are able to confirm the expected velocity of the star

$$v_{\text{pri}} = v_{\text{sys}} - v_{\text{bary}} \quad (1)$$

(where v_{sys} is the systemic velocity of ups And A and v_{bary} is the barycentric velocity of the Earth at the time of observation) as is shown by the strong peaks in the panels on the left-hand side of Figure 4. We suspect that the significant off-peak correlation signature in the primary velocity curve for the K_l band data implies that we were too aggressive in our clipping

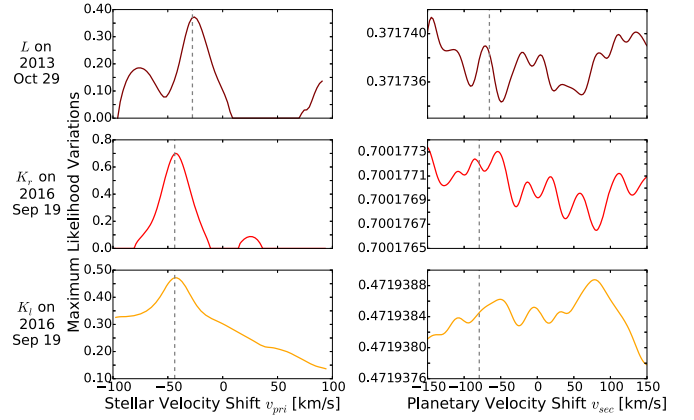


Figure 4. Maximum likelihood functions for selected epochs of data in each band. Panels in the left column show the maximum likelihood function for the velocity shift of the star ups And in each band observed, while panels in the right column show the maximum likelihood function for the velocity shift of the planet ups And b. The gray vertical lines represent the expected values of v_{pri} and v_{sec} (based on the barycentric and systemic velocities and the line-of-sight Keplerian velocity determined in Section 3.4). Based on $\sigma_{f+\omega}$, the error on v_{sec} is 0.4 km s^{-1} .

and that we have scratched the noise limit of our data (see Section 4.4).

The right column of Figure 4 shows the maximum likelihood curves for shifts in the planetary velocity. Two aspects are notable. First, the likelihood variations of the K band data are an order of magnitude smaller than those of the L data, indicative of the small signals present in the K band data. Second, there are many peaks and troughs in the planetary maximum likelihood curves. Therefore, determining the line-of-sight velocity of the planet is not straightforward. Only one peak in each maximum likelihood curve represents the real planetary velocity for a given epoch; the other peaks are chance correlations with the repeating structure in the planetary model. The multi-epoch data are critical in breaking this degeneracy.

3.4. Planet Mass and Orbital Solution

We use the cross-correlation functions for the planetary velocity shift v_{sec} at each epoch to determine the most likely value of the line-of-sight Keplerian velocity K_P . For the sake of completeness, we use the equation for orbital velocity, which considers eccentricity, even though the eccentricity of ups And b is very nearly zero. As a result of this near-zero eccentricity, the mean anomalies M of our observations are essentially the same as the true anomalies f . The velocity v_{sec} of the planet a function of its true anomaly f is

$$v_{\text{sec}}(f) = K_P(\cos(f + \omega) + e \cos \omega) + v_{\text{pri}}, \quad (2)$$

where K_P is the planet's orbital velocity, ω is the longitude of periastron measured from the ascending node, and e is the eccentricity of the orbit. We test orbital velocities from -150 to 150 km s^{-1} in steps of 1 km s^{-1} and thus test a variety of planet masses and orbital inclinations. This results in a plot of maximum log likelihood versus the planet's orbital velocity (first column of Figure 5).

Six L band cross-correlation functions similar to that in the upper right panel of Figure 4 are combined to produce the likelihood curve in the upper left panel of Figure 5 when combined with equal weighting. The single peak in K_P is at $55 \pm 3 \text{ km s}^{-1}$. The error bars reported here are the 3σ error

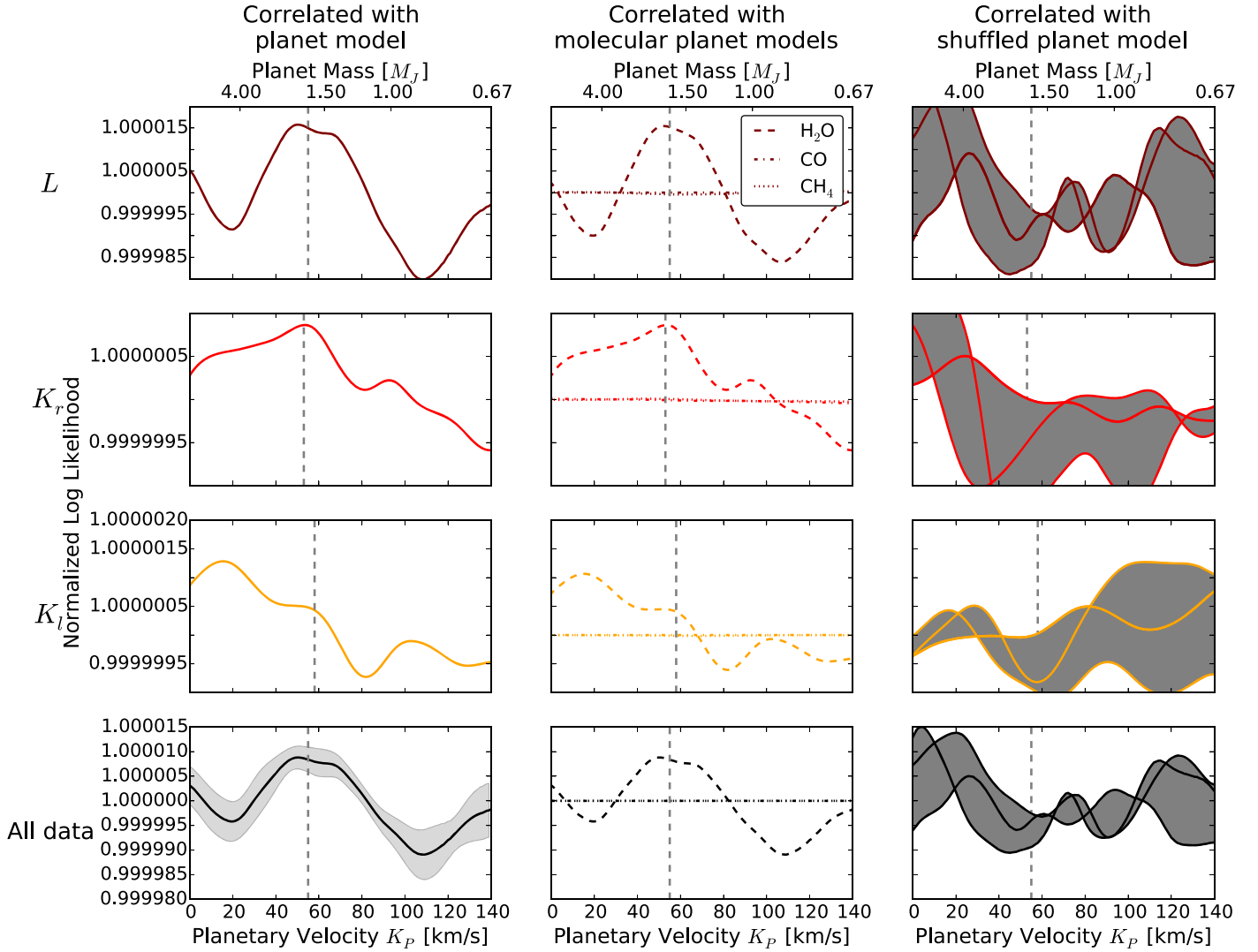


Figure 5. Normalized log likelihood as a function of Keplerian orbital velocity K_p . Note that the vertical axes cannot be directly compared. Likelihood curves in the left column are the result of correlating NIRSPEC data with a SCARLET planet model for ups And b. The light shading on the maximum likelihood curve of all the data correlated with a planet model represent the jackknifed error bars. Likelihood curves in the center column are the result of correlation NIRSPEC data with SCARLET planet models containing single molecules. Likelihood curves in the right column are the result of correlation NIRSPEC data with multiple shuffled SCARLET planet models (which eliminates the planet signal in most cases); the dark shading is for the sake of clarity only. The first row of likelihood curves considers only L band data, the second considers only K_r band data, the third considers only K_l band data, and the fourth considers all of the data.

on the mean value of a Gaussian curve fit to the maximum likelihood peak with equal weighting to the points on the maximum likelihood curve. The error bars are not the full-width at half-maximum of the fitted Gaussian. We more robustly calculate the weighting of the points on the maximum likelihood curve and the error bars and significance of the K_p measurement based on the full 11 nights of data later in this section. Three K_r band cross-correlation functions similar to those in the middle right panel of Figure 4 produce the likelihood curve in the second row of the first column of Figure 5 and shows a peak at $K_p = 53 \pm 3 \text{ km s}^{-1}$. Finally, three K_l band cross-correlation functions similar to that in the bottom right panel of Figure 4 produce the likelihood curve in the third row of the first column of Figure 5 and shows a peak at $K_p = 58 \pm 3 \text{ km s}^{-1}$.

The combination of all nights of data is shown in the bottom left panel of Figure 5 and gives $K_p = 55 \text{ km s}^{-1}$. We use this value of K_p to calculate the expected v_{sec} for each epoch of observation and note this value as a vertical line on the curves

in the right column of Figure 4. For most cases (especially in L and K_r bands), the expected v_{sec} corresponds to a local maximum in likelihood. We also use $K_p = 55 \text{ km s}^{-1}$ to calculate the secondary velocities plotted in Figure 2.

Given the full suite of data, we calculate the error bars of each point of the maximum likelihood curve using jackknife sampling. We remove one night of data from the sample at a time and recalculate the maximum likelihood curve. The error on each point is proportional to the standard deviation of the 12 resulting maximum likelihood curves. These errors are shown in the bottom left panel of Figure 5. These errors are an estimate only. For a Gaussian fit to the peak at 55 km s^{-1} , the reduced chi-squared value (chi-squared divided by the number of degrees of freedom) is 0.15, suggesting that the error bars are likely an overestimate. These large error bars are driven by a high variance in the jackknife samples. The Gaussian fit also gives error bars on the ultimate K_p measurement: $55 \pm 9 \text{ km s}^{-1}$.

To determine the significance of this detection, we use the jackknifed error bars to fit a Gaussian (above) and a straight line and we compare the likelihoods of the fits with the Bayes factor B . Here, the Gaussian fit corresponds to the presence of a planetary signal and the linear fit corresponds to the lack thereof. The Bayes factor B is the ratio of the likelihood of two competing models (Kass & Raftery 1995). If $2\ln B$ is greater than 10, then the model is very strongly preferred.

For the Gaussian fit compared to the linear fit, the value of $2\ln B$ is 10.5, indicating that the signal at 55 km s^{-1} is stronger than a straight line at about 3.7σ . Therefore, the line-of-sight orbital velocity of ups And b is $55 \pm 9 \text{ km s}^{-1}$. Using the indicative mass of ups And b and the law of conservation of momentum, we calculate that the true mass of ups And b is $1.7_{-0.24}^{+0.33} M_J$, and the orbital inclination of ups And b is $24^\circ \pm 4^\circ$.

3.5. Measurements of ups And b's Atmosphere

With SCARLET, we can calculate the contributions of individual molecules (H_2O , CO , and CH_4) to the total spectrum to understand the dominant opacity structures. We cross-correlate these molecular planet models with our L , K_r , and K_l band data. Results of these single molecule cross-correlation calculations are shown in the middle column of Figure 5 for each band observed and indicate that the atmospheric opacity of ups And b is dominated by water vapor at the observed wavelengths. The likelihood curves for data correlated with CO - and CH_4 -only planetary models show variations at least an order of magnitude smaller than the H_2O -only results. If carbon monoxide or methane are present at these wavelengths, they exist at levels below the detection limit of this data set. (See Section 4.3.) Note that we were forced to remove the CO band at $2.2935 \mu\text{m}$ from our data set because of the presence of CO features in the stellar spectrum.

4. Discussion

4.1. Tests of the Orbital Solution

Our initial test of the fidelity of the line-of-sight velocity detection at 55 km s^{-1} is to vary the spectroscopic contrast α_{spec} . We test α_{spec} from 10^{-7} to 10^{-3} and find that the peak at 55 km s^{-1} is robust down to $10^{-6.5}$. α_{spec} is truly the ratio between the depths of the spectral lines, and so could be as low as zero for perfectly isothermal atmospheres.

Analogous to Piskorz et al. (2016), we produce a “shuffled” planetary model by randomly rearranging chunks of the planetary model. Cross-correlating our data with a shuffled model should show no peak near 55 km s^{-1} if the planet truly exists with a line-of-sight orbital velocity of 55 km s^{-1} . For each band of data, we run this test three times and the results are shown in the right-hand column of Figure 5. The L , K_r , and K_l band detections show minima near 55 km s^{-1} , showing that the planet signal is successfully eliminated.

We use our inclination measurement of $24^\circ \pm 4^\circ$ to compare our detection to the results presented in other works. The spectroscopic technique presented here would be unable to detect the motion of ups And b if $i_b < 4.9^\circ$ due to the size of a resolution element on NIRSPEC. Our inclination measurement is largely in agreement with previous works. Spitzer brightness measurements indicated $i_b > 28^\circ$ (Crossfield et al. 2010). Newtonian orbital simulations considering the orbital elements of ups And c and d suggested that orbits having $i_b < 60^\circ$ can

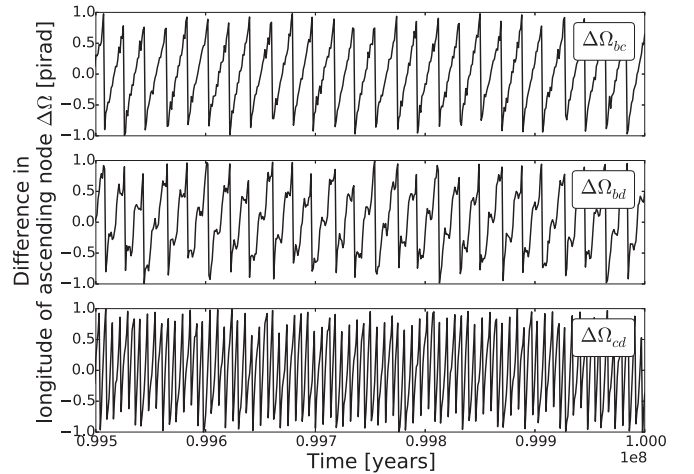


Figure 6. Plot of the difference in longitude of the ascending node $\Delta\Omega$ vs. time for the last 500,000 years of the 100 Myr Mercury simulation for each pair of planets in the ups And system. This simulation was initialized with $i_b = 24^\circ$ and $\Omega_b = 0^\circ$.

be stable (McArthur et al. 2010). Analogous post-Newtonian orbital simulations prescribed a “region of stability” for $i_b < 40^\circ$. Our measurement of $i_b = 24^\circ \pm 4^\circ$ lies within the error bars of these ranges.

4.2. System Stability

Many previous works have characterized the ups And A system as on the edge of instability. Here we evaluate our calculation of the inclination of ups And b by running numerical simulations of the system with the Mercury software (Chambers 1999). Mercury is a hybrid-symplectic-Burlisch Stoeer algorithm (Chambers 1999). We include the central star ups And A and the three planets ups And b, c, and d, set the time step to one-twentieth of the orbital period of ups And b, and consider general relativity.

Our method of calculating K_P and i_b provides no insight into the longitude of the ascending node of ups And b, Ω_b . As a result, we investigate values of i_b between 22° and 27° in steps of 1° and values of Ω_b between 0° and 360° in steps of 10° . We adjust M_b as is necessary given the value of i_b . All other orbital elements are taken from McArthur et al. (2010). Specifically, the orbital elements used for our simulations are listed in Table 1.

Of our 216 simulations, 122 were stable for more than 100,000 years. These simulations have $\Omega_b < 100^\circ$ or $\Omega_b > 260^\circ$. Of these systems, 53 were stable for more than 1 Myr, having $\Omega_b < 40^\circ$ and $\Omega_b > 320^\circ$. We extract the 24 simulations having $23^\circ < i < 25^\circ$ and run them for 100 Myr. All but two are stable. It seems that for the successful simulations the orbital planes of planets b and d remain roughly aligned. For example, if $i_b = 24^\circ$ and $\Omega_b = 0^\circ$, then the mutual inclination of ups And b and c is about 29° and the mutual inclination of ups And b and d is about 2° . Recall that the mutual inclination of ups And c and d is 29° . Successful simulations tend to have mutual inclinations clustered about these values. In these simulations, the apsides of ups And c and d oscillate as in Chiang & Murray (2002), Barnes et al. (2011), and other works, and the orbital evolution of ups And b is secular (Figure 6). We stress that these simulations are stable not necessarily because of the value of ups And b's inclination, but because of the direction ups And b's inclination vector

points over time. Our Mercury simulations provide evidence that stable ups And A systems do indeed exist for the inclination we have measured, and provide insight into the three-dimensional geometry of ups And b’s orbit.

4.3. The Atmosphere of ups And b

In our planetary model, the L band opacity is dominated by water vapor. Therefore, our L band detection of ups And b’s thermal emission spectrum suggests that radiative transfer in the planet’s atmosphere is dominated by water vapor at these wavelengths. In fact, the source of the correlation signal for all wavelengths investigated is water vapor (see the middle column of Figure 5). Based on the analysis of α_{spec} presented in Section 4.1, the detection of H_2O suggests that its spectroscopic contrast $\alpha_{\text{spec}} > 10^{-6.5}$.

We perform a comparison of the cross-correlation results given inverted and non-inverted model spectra. The main differences in the final maximum likelihood curves stem from the different line strengths at a given wavelength for each model. In other words, the differences stem from the optical depths as a function of wavelength. Therefore, the only conclusion we can draw at this time is the atmosphere of ups And b is dominated by water at the probed wavelengths.

Though the K band is typically dominated by CO absorption, the usable K band wavelengths in our data set do not include strong CO absorption. The non-detections of CO and CH_4 suggest that their spectroscopic contrasts are $\alpha_{\text{spec}} < 10^{-6.5}$ at these wavelengths.

Our models do not account for cloud cover, atmospheric recirculation, or the differences between dayside and nightside spectra. Crossfield et al. (2010) reported a flux maximum in the Spitzer phase curve of ups And b at 80° before opposition, or at mean anomaly $M = 0.4$, in our formulation. $M = 0.4$ is almost directly between the phases of 2016 November 12 and 2016 August 21 observations as diagrammed in Figure 1. Fortuitously, this indicates that even if the planet’s flux maximum is shifted from what would traditionally be expected, our measurements are still able to capture dayside emission.

4.4. Observation Notes

From our raw data sets, we calculate the shot noise per resolution element for each observation (see Table 2). We compare the aggregate shot noise values to the expected photometric signal from the planet for each order observed, using the stellar and planet models described in Sections 3.1 and 3.2. As Figure 7 suggests, we easily achieve the required S/N to detect the planet with six nights of L band observations, but only marginally achieve that required with three nights of K_l and K_r observations. In fact, we achieve slightly better shot noise for K_r than for K_l , a possible reason for the stronger detection of the planet signal here (Figures 4 and 5).

In this suite of observations, the K_l band data sets are equivalent to the K band data presented for HD 88133 in Piskorz et al. (2016). With four nights of K band data, Piskorz et al. (2016) were able to detect the signal from HD 88133 b, though not as clearly as in the six nights of L band data. This points to the general trend that, with NIRSPEC at Keck, L band observations may be more amenable to direct detection of exoplanet atmospheres than those in the K band. For hot Jupiters, the increase in the thermal background from K to L band is more than compensated for by the significant increase

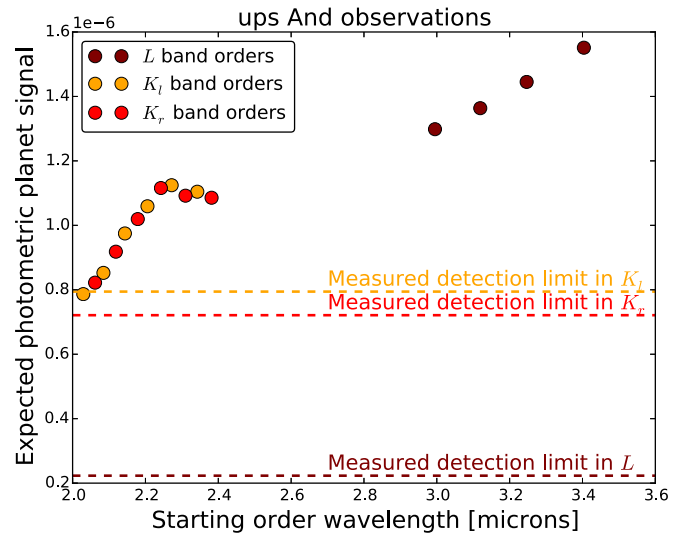


Figure 7. Expected planet–star contrast as a function of starting order wavelength compared to achieved photometric contrast. Points represent the expected planet photometric signal calculated from a PHOENIX stellar model and a SCARLET planet model for each observed order of data (6 orders in K_l , 6 orders in K_r , and 4 orders in L). Dotted lines represent the achievable contrast given by the aggregate shot noise for all epochs of data in each band. Note that in our analysis we do not use the first two and final orders of the K_l and K_r bands.

in planet flux relative to the star. In other words, though the increment of detection limit achieved per unit integration time is higher in the K band than in the L band, the star–planet contrast near $2\ \mu\text{m}$ may be too small for a bona fide planet detection with our data. For this cross-correlation method, the superiority of L band observations over K band observations is a demonstration of the theoretical results presented in de Kok et al. (2014).

5. Conclusion

We detect the thermal emission spectrum of ups And b with ground-based high-resolution spectroscopy. For the hot Jupiter ups And b, we find a Keplerian velocity of $55 \pm 9\ \text{km s}^{-1}$, a true mass of $1.7^{+0.33}_{-0.24}\ M_J$, and an orbital inclination of $24^\circ \pm 4^\circ$. We show that the ups And A system is stable for at least 100 Myr given the reported ups And b orbital elements. Using the many planet lines available in the L and K bands, we determine that the planet’s opacity structure is dominated by water vapor. For the set of observations presented here, the signal is noticeably stronger in the L band than in K , suggesting that L band observations may be best suited for these analyses moving forward. Further thermal IR measurements can be used to dig deeper into the structure and compositions of hot Jupiter atmospheres and eventually atmospheres of planets at larger semimajor axes.

The authors thank an anonymous reviewer for useful comments and suggestions on this paper. The authors also thank Konstantin Batygin for guidance and insight into the stability of this planetary system and wish to recognize and acknowledge the very significant cultural role and reverence that the summit of Maunakea has always had within the indigenous Hawaiian community. We are most fortunate to have the opportunity to conduct observations from this mountain. The data presented herein were obtained at the WM Keck Observatory, which is operated as a scientific partnership among the California Institute

of Technology, the University of California, and the National Aeronautics and Space Administration. The Observatory was made possible by the generous financial support of the WM Keck Foundation. This work was partially supported by funding from the NSF Astronomy & Astrophysics and NASA Exoplanets Research Programs (grants AST-1109857 and NNX16AI14G, G A Blake PI). Basic research in infrared astrophysics at the Naval Research Laboratory is supported by 6.1 base funding.

ORCID

Nathan R. Crockett  <https://orcid.org/0000-0002-6586-7591>

Geoffrey A. Blake  <https://orcid.org/0000-0003-0787-1610>

Travis S. Barman  <https://orcid.org/0000-0002-7129-3002>

Chad F. Bender  <https://orcid.org/0000-0003-4384-7220>

John S. Carr  <https://orcid.org/0000-0002-6695-3977>

References

- Adams, F. C., & Laughlin, G. 2006, *JMPD*, **15**, 2133
- Asplund, M., Grevesse, N., Suval, J. A., & Scott, P. 2009, *ARA&A*, **47**, 481
- Barnes, R., & Greenberg, R. 2006, *ApJL*, **652**, L53
- Barnes, R., & Greenberg, R. 2007, *ApJL*, **659**, L53
- Barnes, R., Greenberg, R., Quinn, T. R., et al. 2011, *ApJ*, **726**, 71
- Benneke, B. 2015, arXiv:1504.07655
- Birkby, J. L., de Kok, R. J., Brogi, M., et al. 2013, *MNRAS*, **436**, L35
- Boogert, A. C. A., Blake, G. A., & Tielens, A. G. G. M. 2002, *ApJ*, **577**, 271
- Borysow, A. 2002, *A&A*, **390**, 779
- Brogi, M., de Kok, R. J., Albrecht, S., et al. 2016, *ApJ*, **817**, 106
- Brogi, M., de Kok, R. J., Birkby, J. L., Schwarz, H., & Snellen, I. A. G. 2014, *A&A*, **565A**, 124B
- Brogi, M., Snellen, I. A. G., de Kok, R. J., et al. 2012, *Natur*, **486**, 502
- Brogi, M., Snellen, I. A. G., de Kok, R. J., et al. 2013, *ApJ*, **767**, 1
- Burrows, A., & Volobuyev, M. 2003, *ApJ*, **583**, 985
- Butler, R. P., Marcy, G. W., Fisher, D. A., et al. 1999, *ApJ*, **526**, 916
- Butler, R. P., Marcy, G. W., Williams, E., et al. 1997, *ApJL*, **474**, L115
- Chambers, J. E. 1999, *MNRAS*, **304**, 793
- Chiang, E. I., & Murray, N. 2002, *ApJ*, **576**, 1
- Claret, A. 2000, *A&A*, **363**, 1081
- Crossfield, I. J. M., Hansen, B. M. S., Harrington, J., et al. 2010, *ApJ*, **723**, 1436
- Curiel, S., et al. 2011, *A&A*, **525**, A78
- de Kok, R. J., Birkby, J., Brogi, M., et al. 2014, *A&A*, **561**, A150
- de Kok, R. J., Brogi, M., Snellen, I. A. G., et al. 2013, *A&A*, **554**, A82
- de Mooij, E. J. W., Brogi, M., de Kok, R. J., et al. 2012, *A&A*, **538**, A46
- Dietrick, R., Barnes, R., McArthur, B., et al. 2015, *ApJ*, **798**, 46
- Fischer, D. A., Marcy, G. W., & Spronck, J. F. P. 2014, *ApJSS*, **210**, 1
- Gonzalez, G., & Laws, C. 2007, *MNRAS*, **278**, 1141
- Harrington, J., Hansen, B. M., Luszcz, S. H., et al. 2006, *Sci*, **314**, 623
- Husser, T.-O., Wende-von Berg, S., Dreizler, S., et al. 2013, *A&A*, **553**, A6
- Kass, R. E., & Raftery, A. E. 1995, *JASA*, **90**, 773
- Lissauer, J. J., & Rivera, E. J. 2001, *ApJ*, **554**, 1141
- Lockwood, A. C., Johnson, J. A., Bender, C. F., et al. 2014, *ApJL*, **783**, L29
- Lowrance, P. J., Kirkpatrick, J. D., & Beichman, C. A. 2002, *ApJL*, **572**, L79
- Martins, J. H. C., Santos, N. C., Figueira, P., et al. 2015, *A&A*, **576**, A134
- McArthur, B. E., Benedict, G. F., Barnes, R., et al. 2010, *ApJ*, **715**, 1203
- McLean, I. S., Becklin, E. E., Bendiksen, O., et al. 1998, *Proc. SPIE*, **3354**, 566
- Nagasawa, M., Ida, S., & Bessho, T. 2008, *ApJ*, **678**, 498
- Nidever, D. L., Marcy, G. S., Butler, R. P., et al. 2002, *ApJSS*, **141**, 503
- Piskorz, D., Benneke, B., Crockett, N. R., et al. 2016, *ApJ*, **832**, 2
- Piskunov, N. E., Kupka, F., Ryabchikova, T. A., Weiss, W. W., & Jeffery, C. S. 1995, *A&AS*, **112**, 525
- Rivera, E. J., & Lissauer, J. J. 2000, *ApJ*, **530**, 454
- Rodler, F., Lopez-Morales, M., & Ribas, I. 2012, *ApJL*, **753**, L25
- Rothman, L. S., Gordon, I. E., Barbe, A., et al. 2009, *JQSRT*, **110**, 533
- Schwarz, H., Brogi, M., deKok, R. J., et al. 2015, *A&A*, **579**, A111
- Snellen, I. A. G., Brandl, B. R., deKok, R. J., et al. 2014, *Natur*, **503**, 63
- Snellen, I. A. G., de Kok, R. J., de Mooij, E. J. W., & Albrecht, S. 2010, *Natur*, **465**, 1049
- Takeda, G., Ford, E. B., Sills, A., et al. 2007, *ApJS*, **168**, 297
- Tennyson, J., & Yurchenko, S. N. 2012, *MNRAS*, **425**, 21
- Valenti, J. A., Butler, R. P., & Marcy, G. W. 1995, *PASP*, **107**, 966
- Valenti, J. A., & Fischer, D. A. 2005, *ApJSS*, **189**, 141
- vanBelle, G. T., & vonBraun, K. 2009, *ApJ*, **694**, 1085
- Wright, J. T., Upadhyay, S., Marcy, G. W., et al. 2009, *ApJ*, **693**, 1084
- Zucker, S., & Mazeh, T. 1994, *ApJ*, **420**, 806